Available online at www.sciencedirect.com
ScienceDirect
Journal of Solid State Chemistry 179 (2006) 3295–3307
JOURNAL OF SOLID STATE CHEMISTRY
www.elsevier.com/locate/jssc

A conjoint XRD–ND analysis of the crystal structures of austenitic and martensitic $Ti_{0.64}Zr_{0.36}Ni$ hydrides

F. Cuevas[a,*], M. Latroche[a], F. Bourée-Vigneron[b], A. Percheron-Guégan[a]

[a]LCMTR-ISCSA-CNRS, 2-8 rue Henri Dunant, 94320 Thiais Cedex, France
[b]LLB, CEA-CNRS, CE-Saclay, 91191 Gif sur Yvette Cedex, France

Received 9 September 2005; received in revised form 16 June 2006; accepted 18 June 2006
Available online 29 June 2006

Abstract

The crystal structures of the hydrides of austenitic and martensitic $Ti_{0.64}Zr_{0.36}Ni$ alloy have been investigated by conjoint X-ray diffraction (XRD)–neutron diffraction (ND) analysis. Austenitic $Ti_{0.64}Zr_{0.36}Ni$ alloy with cubic CsCl-type structure preserves its metal sublattice structure after deuteration. It forms a $Ti_{0.64}Zr_{0.36}NiD_{1.5}$ deuteride with D-atoms occupying half of the octahedrally coordinated 3*d* sites. On the contrary, the monoclinic TiNi-type structure of martensitic $Ti_{0.64}Zr_{0.36}Ni$ alloy is modified after deuterium absorption. At $P_{D2} = 10^3$ Pa and $T = 298$ K, two deuterides coexist with orthorhombic CrB-type structure for the metal sublattice and compositions $Ti_{0.64}Zr_{0.36}NiD$ (β-deuteride) and $Ti_{0.64}Zr_{0.36}NiD_{2.6}$ (γ-deuteride). For the β-monodeuteride, deuterium atoms are tetrahedrally coordinated by (Ti,Zr) atoms. For the γ-deuteride, D-atoms fully occupy tetrahedrally coordinated $(Ti,Zr)_3Ni$ 8*f* sites and partially occupy pyramidal $(Ti,Zr)_3Ni_2$ 4*c* sites. At higher pressures, deuterium solution occurs in the γ-phase with a partial occupancy of octahedrally coordinated $(Ti,Zr)_2Ni_4$ 4*a* sites.

Keywords: Intermetallics; Martensitic transformation; Hydrogen storage materials; Crystal structure and symmetry; X-ray diffraction; Neutron diffraction

1. Introduction

TiNi is an outstanding alloy due to both shape memory behavior and hydrogen uptake capability [1–4]. Its shape memory effect is allowed by a martensitic transformation (MT) between a high temperature phase of cubic symmetry and a low temperature phase of monoclinic symmetry [5,6]. MT is a first order and diffusionless reversible transition with thermal hysteresis. By analogy with steels, high and low temperature phases in TiNi are denoted as austenite and martensite, respectively. For equiatomic TiNi, the martensite starts to nucleate on cooling at $T \sim 310$ K, whereas the reverse transformation starts at $T \sim 340$ K [7]. Nevertheless, MT temperatures are strongly dependent on the chemistry (stoichiometry [7], metal substitutions [8] and impurity gas content [9]) and the thermo-mechanical history [10,11] of the alloy.

The crystal structure of TiNi austenite was determined long time ago [12]. It has a cubic B2 CsCl-type structure (space group (SG) $Pm\bar{3}m$, Ni 1*a* (0,0,0) ,Ti 1*b* (1/2, 1/2, 1/2)) with lattice parameter $a = 3.015$ Å [13]. The crystal structure determination of TiNi martensite has been much problematic due to its complex structure and the difficulty of obtaining randomly oriented powder samples [14,15]. It is now widely accepted that its crystal structure is monoclinic B19′ $P2_1/m$ (Ti 2*e* (0.4176, 1/4, 0.2164), Ni 2*e* (0.0372, 1/4, 0.6752)) with lattice parameters $a = 2.898$ Å, $b = 4.108$ Å, $c = 4.646$ Å and $\beta = 97.78°$, as established by Kudoh et al. [16] by single crystal X-ray diffraction.

Hydrogenation properties of TiNi austenite as refers to pressure–composition isotherms (PCI) have been determined by Burch and Mason [17]. TiNi absorbs up to 1.2 hydrogen atoms per *AB* formula unit (H/*AB*, *A* = Ti, *B* = Ni) at 400 K and 1 MPa of hydrogen pressure. H-absorption takes place without showing any evidence of a pressure invariant plateau region at $P > 0.02$ MPa. This may suggest that hydrogen enters as a solution phase, a statement that should be discarded after structural data of

*Corresponding author. Fax: +33 1 4978 1203.
E-mail address: fermin.cuevas@glvt-cnrs.fr (F. Cuevas).

0022-4596/$ - see front matter © 2006 Elsevier Inc. All rights reserved.
doi:10.1016/j.jssc.2006.06.025

Noréus et al. [18] and Soubeyroux et al. [19]. In fact, hydrogen absorption induces a tetragonal distortion of the cubic alloy matrix forming a $(2a \times 4a)$ supercell structure. Unit-cell parameters for $TiNiH_{1.4}$ hydride are reported to be $a = 6.2365$ Å and $c = 12.424$ Å, leading to a 10% cell volume expansion with respect to the parent alloy. H-atoms almost occupy half of the octahedral Ti_4Ni_2 sites available in the metal sublattice.

As regards to the hydrogenation properties of TiNi martensite, scarce information is reported in the literature. This should be related to the difficulty of producing bulk specimens of martensitic-derived hydrides. The reasons of this are manifold. First, the martensitic phase only holds near or below room temperature, where H-diffusivity is sluggish. Secondly, TiNi alloy is extremely tough and, therefore, difficult to obtain in powder state for being hydrogenated in a reasonable time. Finally, solid-gas hydrogen absorption in TiNi alloy is easily hampered due to the formation of surface oxides. As a consequence, martensite hydrogenation has been mostly performed by electrochemical loading and the reported data only concerns modifications of the MT behavior in TiNi alloy by H-uptake [20]. Therefore, these studies do not provide fundamental results on the main hydrogenation properties (i.e., H-thermodynamics and hydride crystal structure) for the martensitic phase.

In this paper, a conjoint X-ray diffraction (XRD)–neutron diffraction (ND) study was done in order to determine the crystal structures of $Ti_{0.64}Zr_{0.36}Ni$ deuterides. Zr-substituted $Ti_{0.64}Zr_{0.36}Ni$ alloy has been used since it allows the hydrogenation of bulk martensitic alloy up to 400 K [21]. Deuterium is used instead of hydrogen to avoid the incoherent scattering contribution of the latter for ND experiments. Structural determination of this system demands both techniques since, on the one hand, hydrogen does not contribute significantly to XRD and, on the other hand, expected zirconium substitution in titanium sites with a 0.36/0.64 ratio results in a very low averaged scattering amplitude for ND (0.038×10^{-12} cm) due to the opposite signs of Ti and Zr atoms. In fact, Sidhu et al. [22] utilized disordered $Ti_{0.62}Zr_{0.38}$ alloys to determine deuterium location with zero scattering amplitude for metal atoms. A short report of this study based only on XRD data has been published in the frame of the MH2004 Conference [23].

2. Experimental

2.1. Alloy elaboration and chemical analysis

Two Zr-substituted TiNi-type alloy ingots with nominal composition $Ti_{0.64}Zr_{0.36}Ni$ were elaborated by induction melting from the pure elements (purity 99.95%). The ingots were melted five times under secondary vacuum and turned over between each melting to ensure their homogeneity. One of them was subsequently annealed at 1273 K for 2 weeks under argon atmosphere. Alloy composition was analyzed by electron probe microanalysis (EPMA) in a Cameca SX-100 instrument operated at 15 kV. The induction-melted alloy shows a major phase (98 wt%) of composition $Ti_{0.64(1)}Zr_{0.34(1)}Ni_{1.02(1)}$ and minor $(Ti,Zr)_2Ni$-type precipitates (2 wt%), as evaluated from graphical analysis of scanning electron microscopy images. The second alloy ingot was melt-spun under helium atmosphere over a stainless-steel wheel having a surface velocity of 19 m/s. This sample was obtained as a flat ribbon 40 μm in thickness. The melt-spun alloy is chemically homogeneous with composition $Ti_{0.656(2)}Zr_{0.350(2)}Ni_{0.994(2)}$. These two alloys will be referred to as "annealed" and "melt-spun" alloys, respectively.

2.2. Alloy crystal structure vs. elaboration route

The crystal structures for annealed and melt-spun alloys were analyzed at room temperature by X-ray diffraction (XRD) in a θ–θ diffractometer (Bruker AXS D8Advance equipped with backscattered rear graphite monochromator) using Cu$K\alpha$ radiation (Fig. 1). A step size of 0.02° was used. The alloys are very tough so that XRD data were initially obtained for bulky samples, which hamper the full determination of the crystal structure by powder diffraction. Nevertheless, diffraction peaks from the annealed alloy could be indexed to the martensitic TiNi-type monoclinic structure (SG $P2_1/m$) with cell parameters $a = 3.057(1)$ Å, $b = 4.093(1)$ Å, $c = 4.887(1)$ Å and $\beta = 103.17(1)°$. A tiny additional diffraction line could be observed at $2\theta = 40.2°$, which is attributed to the Ti_2Ni-type secondary phase. As for the melt-spun alloy, all XRD peaks are indexed to the austenitic CsCl-type cubic structure (SG $Pm\bar{3}m$) with cell parameter $a = 3.0826(2)$ Å. A wide diffraction halo at $2\theta \sim 40°$ reveals the formation of minor amorphous phase in the melt-spun sample.

Phase stability of both alloys was studied above room temperature by differential scanning calorimetry (DSC) in a Q100 device from TA instruments. Runs were performed at 10 K/min under argon flow (Fig. 2). The annealed alloy undergoes forward and reverse MTs at peak temperatures of 402 and 422 K, respectively. On the contrary, no MT is detected for the melt-spun alloy, as expected from the fact that the alloy is in austenitic state at room temperature. However, an exothermic peak with reaction enthalpy of 0.94 kJ/mol was observed at 777 K, which is related to the crystallization of the amorphous phase as determined from subsequent XRD measurements. As the austenitic-type alloy is obtained by a non-equilibrium route, i.e. melt-spinning, this phase is thought to be metastable at room temperature.

2.3. Hydrogenation properties and preparation of deuterides

Solid-gas PCI for both alloys have been described in detail in previous publications [21,24]. We only report here the necessary data to select and ascertain the deuterium content of the samples for structural analysis. PCI

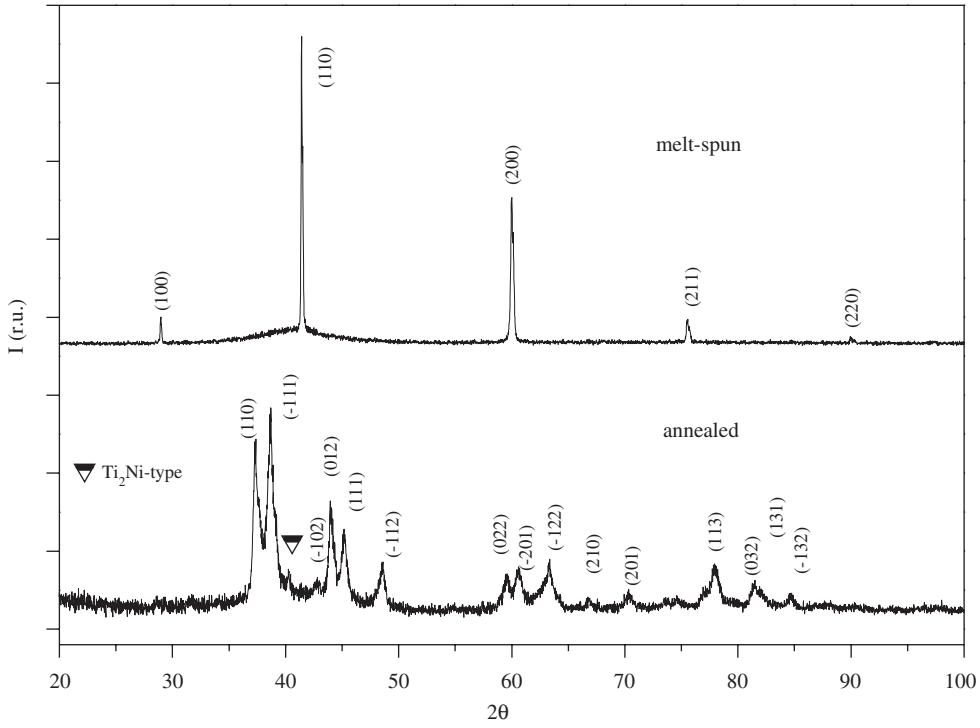

Fig. 1. XRD data of "annealed" and "melt-spun" $Ti_{0.64}Zr_{0.36}Ni$ alloys. Diffraction peaks for the "annealed" alloy are indexed to a monoclinic $P2_1/m$ structure and those for the "melt-spun" alloy are indexed to a cubic $Pm\bar{3}m$ structure. Ti_2Ni impurity reflections for the "annealed" alloy are expressly indicated.

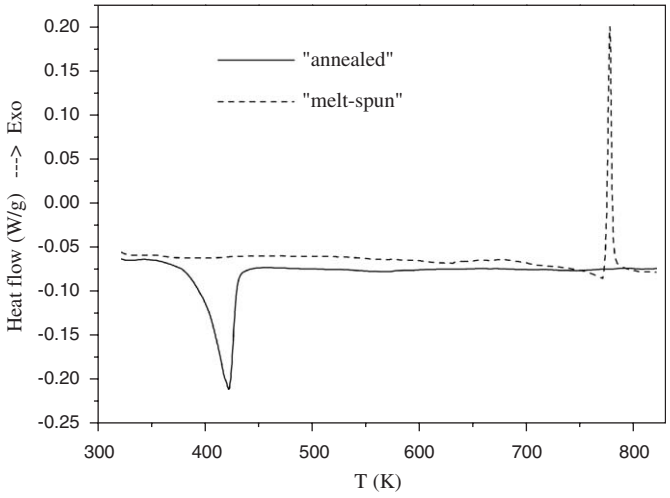

Fig. 2. DSC heating runs for "annealed" and "melt-spun" alloys.

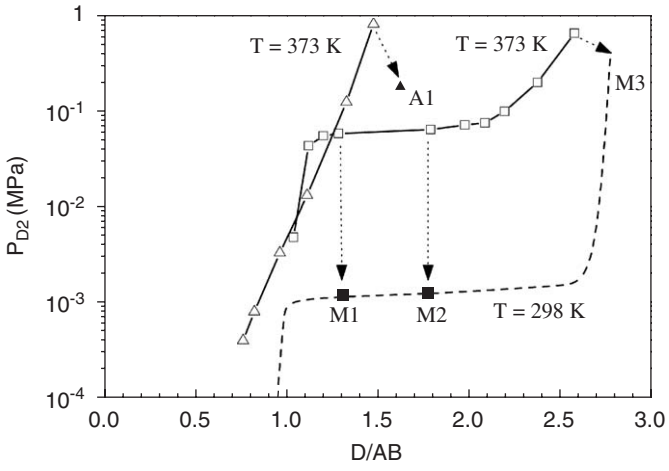

Fig. 3. PCI absorption curves at 373 K for "annealed" (□) and "melt-spun" (△) $Ti_{0.64}Zr_{0.36}Ni$ alloys. *P–C* paths on cooling to room temperature (■, ▲) are shown by dotted lines for every sample studied in this work. The room temperature PCI, depicted by a dashed line, was obtained from ND results for deuterium content and from solid-gas measurements for deuterium pressure.

absorption curves at 373 K for both alloys were obtained by the Sievert's method and are shown in Fig. 3. "Melt-spun" austenitic alloy forms $ABD_{1.5}$ β-deuteride at 1 MPa with no plateau pressure. On the contrary, "annealed" martensitic alloy absorbs up to 2.6 D/*AB* at the same pressure while displaying a flat plateau pressure at 0.06 MPa. This plateau reveals the existence of two deuteride phases, which will be denoted as β- and γ-deuteride phases. In order to study the crystal structures of these deuterides, four samples were cooled down to room temperature under deuterium atmosphere (dotted lines in Fig. 3). For the determination of the β-austenitic deuteride, a sample (A1) with concentration 1.60(5) D/*AB* was elaborated. As for the martensite, three deuterides were prepared with compositions at the beginning of the plateau (M1), at mid-plateau (M2) and at the maximum attained pressure, 0.35 MPa (M3). The resulting alloy compositions are D/*AB* = 1.3(1), 1.8(1) and 2.75(5), respectively.

Crystal structures for the deuterides were studied at room temperature by powder XRD and ND. ND experiments

were recorded over the range 6–125° by steps of 0.05° on the diffractometer 3T2 at the LLB in Saclay. The wavelength was set to 1.225 Å. Samples for ND were introduced into a silica tube container that produces a significant background contribution but no diffraction lines. XRD and ND data were conjointly refined by the Rietveld method using the Fullprof program [25]. The used scattering amplitudes ($\times 10^{12}$ cm) are $b_{Ni} = 1.03$, $b_{Ti} = -0.3438$, $b_{Zr} = 0.716$ and $b_D = 0.6671$. The well established Switendick and Westlake criteria have been considered to allow for deuterium location in a particular interstitial site. The Switendick criterion states that the minimum distance between H atoms is of 2.1 Å due to electrostatic repulsion [26]. Owing to empirical geometric considerations, the Westlake criterion requires a minimum interstitial hole radius of 0.37 Å to hold H atoms [27]. For the evaluation of the interstitial sizes, the following element radii have been used: $r_{Ni} = 1.24$ Å, $r_{Ti} = 1.47$ Å and $r_{Zr} = 1.60$ Å. When considering randomly substitution of Zr in Ti sites, an average radius of $r_{(Ti,Zr)} = 1.52$ Å is used for the site composition $Ti_{0.64}Zr_{0.36}$.

3. Results

3.1. Crystal structures of the intermetallic compounds

As mentioned before, powders from the starting alloys are difficult to obtain. However, the alloys become brittle after deuteration. As a matter of fact, the annealed martensitic alloy pulverizes spontaneously, whereas extended cracks are developed in the melt-spun austenitic alloy. Such embrittlement facilitates the elaboration of deuterated powders. These samples were then thermally degassed to obtain D-free alloys for powder XRD analysis. Desorption was performed under secondary vacuum up to 603 and 733 K for the martensitic and austenitic alloys, respectively. Rietveld refinements of XRD patterns for both degassed alloys are shown in Fig. 4. The results of the refinement are summarized in Table 1.

For the martensitic alloy, besides the monoclinic martensitic phase, two secondary phases are detected: an austenitic-type (Ti,Zr)Ni (7 wt%) phase and $(Ti,Zr)_2Ni$ phase (3 wt%). No hydride phase remains in the sample after hydrogen desorption. The unit cell-volume of the desorbed martensitic phase (59.49(2) Å^3) agrees with that measured for the starting alloy (59.55(2) Å^3). The amount of $(Ti,Zr)_2Ni$ phase concurs with that found by EPMA for the starting alloy. As concerns the minor austenitic phase, its occurrence is explained by the reverse MT during degassing at high temperatures. The high temperature phase is retained after cooling to room temperature.

$Ti_{0.64}Zr_{0.36}Ni$ martensite has the same crystal symmetry as TiNi martensite [16]. Main effects of Zr-substitution are an expansion of the unit cell volume (8.5%) and the increase of the monoclinic distortion (β-angle changes from 97.78° to 103.75°). The variation of the lattice parameters is anisotropic. The a and c lattice parameters are observed to increase with Zr-content, whereas the b parameter decreases slightly. This result concurs with previous XRD data reported by Hsieh and Wu [28] for $Ti_{50.5-x}Zr_xNi_{49.5}$ alloys. Anisotropic line broadening with broad ($h0l$)

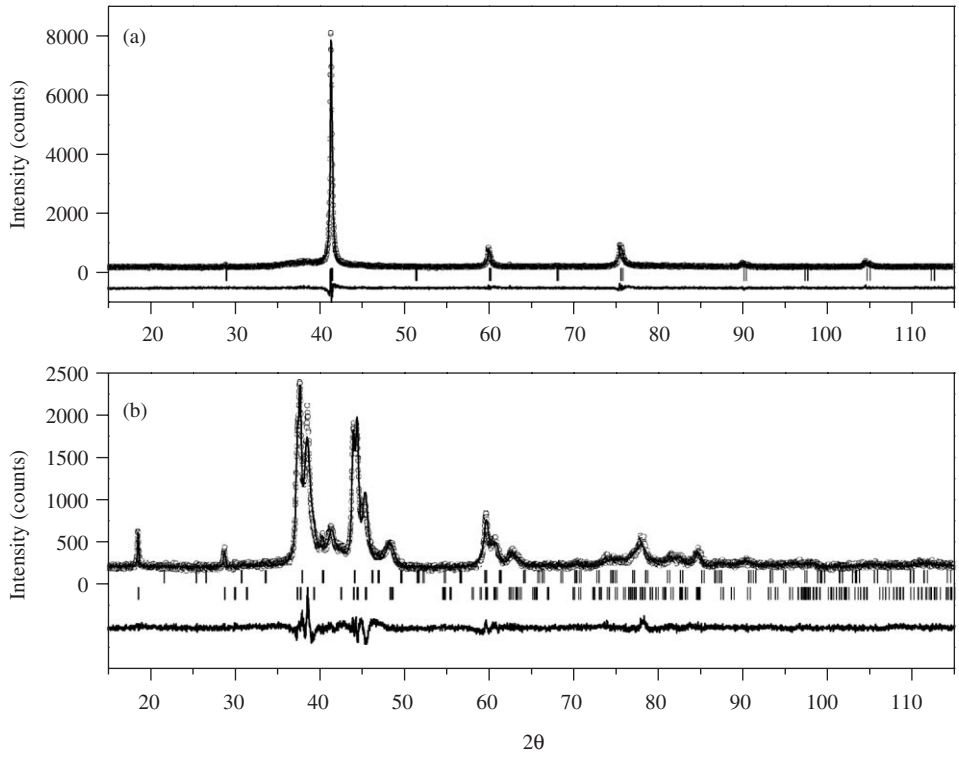

Fig. 4. XRD data and Rietveld analysis of (a) austenitic and (b) martensitic $Ti_{0.64}Zr_{0.36}Ni$ alloys after thermal desorption. Calculated diffraction pattern (continuous line), diffraction line positions (vertical bars) and difference curve at the same scale (below) are given.

Table 1
Structural data for thermally degassed martensitic and austenitic $Ti_{0.64}Zr_{0.36}Ni$ alloys

Atom	Site	x	y	z	B (Å^2)	occ	Atom	Site	x	y	z	B (Å^2)	occ
Martensitic $Ti_{0.64}Zr_{0.36}Ni$ alloy							*TiNi-martensite [16]*						
Ni	2*e*	0.057(1)	1/4	0.669(1)	1.2*	2	Ni	2*e*	0.0372(4)	1/4	0.6752(2)	0.99	2
Ti	2*e*	0.389(1)	1/4	0.213(1)	0.3(1)	1.28	Ti	2*e*	0.4176(5)	1/4	0.2164(3)	0.84	2
Zr	2*e*	0.389(1)	1/4	0.213(1)	0.3(1)	0.72							
	*Anisotropic $B_{Ni}(\times 10^4)$: $\beta_{11} = 1030(60)$, $\beta_{22} = 100(20)$, $\beta_{33} = -22(15)$, $\beta_{13} = 250(20)$												
$P2_1/m$, $Z = 2$							$P2_1/m$, $Z = 2$						
$a = 3.0639(4)$ Å		$b = 4.0737(4)$ Å			$c = 4.9078(6)$ Å		$a = 2.898(1)$ Å		$b = 4.108(2)$ Å			$c = 4.646(3)$ Å	
	$\beta = 103.80(1)^\circ$		$V = 59.49(2)$ Å^3					$\beta = 97.78(4)^\circ$		$V = 54.79(4)$ Å^3			
	Saa = 8.5(5), Sbb = 0, Scc = 0, Sdd = 26.4(3)												
Secondary phases													
$Pm\bar{3}m$ (Ti,Zr)Ni-austenite			7(1) wt%		$a = 3.081(1)$ Å								
$Fd3m$ $(Ti,Zr)_2Ni$-type			3(1) wt%		$a = 11.611(4)$ Å								
R_{wp}	R_p	R_B*	χ^2	N_{ref}*	*Main phase								
7.8%	6.1%	3.75%	1.99	117	26 variables								
Austenitic $Ti_{0.64}Zr_{0.36}Ni$ alloy							*TiNi-austenite [13]*						
Ni	1*a*	0	0	0	3.0(1)	1	Ni	1*a*	0	0	0	Not given	1
Ti	1*b*	1/2	1/2	1/2	2.4(1)	0.64	Ti	1*b*	1/2	1/2	1/2	Not given	1
Zr	1*b*	1/2	1/2	1/2	2.4(1)	0.36							
$Pm\bar{3}m$, $Z = 1$		$a = 3.0780(2)$ Å			$V = 29.162(3)$ Å^3		$Pm\bar{3}m$, $Z = 1$		$a = 3.015(1)$ Å			$V = 27.41$ Å^3	
R_{wp}	R_p	R_B	χ^2	N_{ref}									
7.29%	5.84%	3.60%	1.67	12	9 variables								

Atomic coordinates (x, y, z), Displacement factors (B), occupancy factors (occ), Strain parameters (S) and reliability factors (R_{wp}%, R_p, R_B and χ^2). Standard deviations referred to the last significant digits are given in parentheses. Published data for both martensitic and austenitic phases in binary TiNi alloy are given for comparison.

reflections as compared with (0*kl*) ones was taking into account using the model described by Rodríguez-Carvajal et al. [29]. Fluctuations are observed for the *a*-parameter (Saa = 8.5(5)) and the β-angle (Sdd = 26.4(3)). These fluctuations are related either to chemical inhomogeneity between Ti and Zr atoms or to the hydrogenation/dehydrogenation treatment. Anisotropic displacement factor was noted for the Ni atom along the *a*-axis ($\beta_{11} = 1030$, $\beta_{22} = 100$, $\beta_{33} = -22$, $\beta_{13} = 250$) though this result should be taken cautiously due to low accuracy of powder XRD to determine displacement factors. Nevertheless, as will be later reported, such anisotropic displacement for Ni atoms is also observed in ND data from deuterated samples, indicating a delocalization of Ni atoms along the *a*-axis. It is also worth noting that *x*-positions of both (Ti,Zr) and Ni atoms vary significantly as compared to the binary alloy whereas *z*-positions are nearly identical. All these observations, i.e. lattice parameters, microstrains, displacement factors and change in atomic positions indicate that Zr by Ti substitution produces strong anisotropic effects along the *a*-axis of the monoclinic unit cell.

As concerns to the "melt-spun" alloy, XRD data is well-fitted with a CsCl-type structure. Zr-substitution induces a cell volume expansion of 6.4%. The isotropic Debye–Waller factors are large for all atoms (2–3 Å^2), a fact widely reported in the literature for austenitic TiNi [4,13]. This is currently attributed either to a soft phonon mode that precedes the MT or to incomplete long-range ordering related to the melt-spinning process. For Zr-substituted alloys, the chemical disorder induced by the substitution may also contribute significantly to this effect. Cell-volume expansion in both austenitic and martensitic structures is due to the difference of atomic radii between Ti and Zr atoms. For both structures, Ti and Zr atoms statistically occupy the same site, forming a (Ti,Zr) pseudo-atom with composition $Ti_{0.64}Zr_{0.36}$. We report once for all that such a random substitution is preserved for all deuteride samples analyzed in this study.

3.2. Crystal structure of austenitic deuteride (A1 sample)

The conjoint XRD–ND Rietveld analysis of the austenitic-derived deuteride is shown in Fig. 5 and the results are summarized in Table 2. The metal sublattice preserves the CsCl-type structure upon deuteration with a cell volume expansion of 10.4% with respect to the parent $Ti_{0.64}Zr_{0.36}Ni$ alloy. The refined D-content is slightly lower than that determined by the volumetric method (D/*AB* = 1.50(3) and 1.60(5), respectively), which is reasonable due to expected deuterium uptake into the secondary amorphous phase. Deuterium atoms are located in Wyckoff positions 3*d*, i.e. in octahedral sites with $(Ti,Zr)_4Ni_2$ neighbors, with half of the maximum occupancy (Fig. 6). No deuterium was found in octahedral 3*c* sites. The distance from D to Ni first neighbors is quite short (1.59 Å) in comparison with that to Ti and the closest D atoms (2.25 Å for both). As a consequence, the hole radius between Ni atoms is only of 0.35 Å, whereas that between Zr atoms is as large as 0.73 Å. The isotropic temperature *B*-factors are very high, specially for Ni and D atoms (6.1

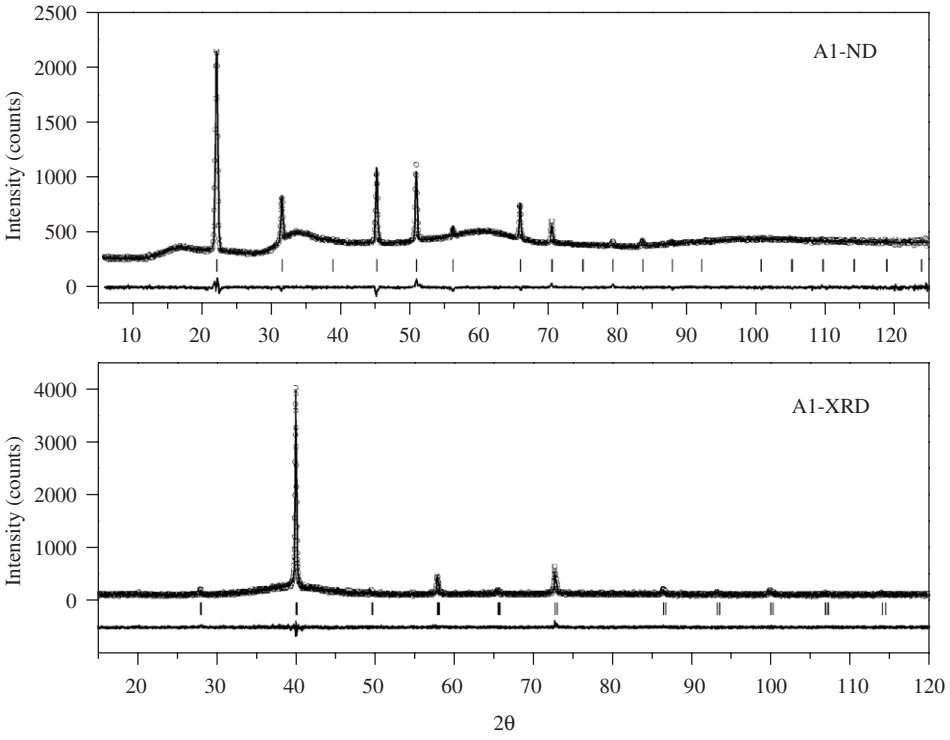

Fig. 5. Conjoint ND and XRD Rietveld analysis of austenitic $Ti_{0.64}Zr_{0.36}NiD_{1.6}$ sample (A1). Calculated diffraction pattern (continuous line), diffraction line positions (vertical bars) and difference curve at the same scale (below) are given.

Table 2
Structural data for austenitic $Ti_{0.64}Zr_{0.36}NiD_{1.5}$ deuteride (A1 sample)

Atom	Site	x	y	z	B (Å^2)	occ
Ni	1*a*	0	0	0	6.1(2)	1 (fixed)
Ti	1*b*	1/2	1/2	1/2	2.4(2)	0.64 (fixed)
Zr	1*b*	1/2	1/2	1/2	2.4(2)	0.36 (fixed)
D	3*d*	1/2	0	0	4.1(1)	1.50(3)
	R_{wp}	R_p	R_B	χ^2	N_{ref}	
ND	1.78	1.38	7.82	1.77	23	
XRD	8.7	6.81	7.5	1.12	12	
18 variables	$Pm\bar{3}m$, $Z=1$	$a = 3.1818(2)$ Å, $V = 32.212(4)$ Å^3				

Atomic coordinates (x, y, z), displacement factors (B), occupancy factors (occ) and reliability factors (R_{wp}, R_p, R_B and χ^2). Standard deviations referred to the last significant digits are given in parentheses.

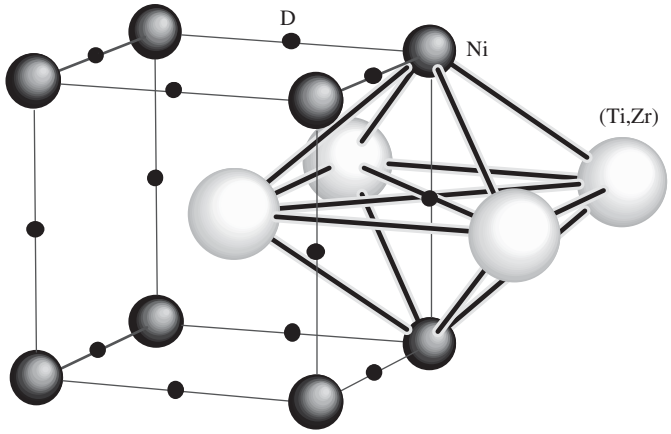

Fig. 6. Crystal structure of austenitic $Ti_{0.64}Zr_{0.36}NiD_{1.5}$ deuteride. Two (Ti,Zr) atoms from an adjacent unit cell have been included to show the octahedral coordination of D atoms. Only half of the sites depicted for D-atoms are occupied.

and 4.1 Å^2, respectively) indicating a highly disordered structure.

3.3. Crystal structure of martensitic deuterides (M1–M3 samples)

The conjoint XRD–ND Rietveld analyses of the martensitic-derived deuterides within the two-phase plateau region (samples M1 and M2) are shown in Figs. 7 and 8, respectively. As expected, both samples are well refined with two deuteride phases having distinct deuterium contents. Such deuterides are denoted in the following as β and γ phases for D-poor and D-rich phases, respectively. The monoclinic symmetry of the parent alloy is modified since both deuterides crystallize in the orthorhombic symmetry (SG *Cmcm*). The sole difference between M1 and M2 samples is the relative phase abundance. M1 sample consists of β and γ phases with a mass fraction of 76(2)% and 24(2)%, respectively, whereas those of the M2 sample are 54(2)% and 46(2)%, respectively. The sample deuterium content as refined by ND (1.39(5) and 1.87(5) D/*AB* for M1 and M2 samples, respectively) agrees with those obtained by the volumetric method (1.3(1) and 1.8(1) D/*AB* for M1 and M2 samples, respectively). For the sake of simplicity, the crystal structure of both deuterides is described in the following using the Rietveld results obtained from sample M2.

The results of the Rietveld analysis for the M2 sample are summarized in Table 3 and the determined structures for β and γ deuteride phases are shown in Fig. 9. For both phases, the metal sublattice is orthorhombic CrB-type. Ni and (Ti,Zr) atoms occupy in both phases Wyckoff positions 4*c* (0, y, 1/4) with $y_{(Ti,Zr)} \sim 0.145$ and $y_{Ni} \sim 0.430$. The main difference between β and γ phases lies in their lattice parameters and unit-cell volume due to their distinct deuterium contents. Normalized cell-volumes (V/AB) are 31.34 and 35.21 Å^3 for β and γ phases, respectively, which represents a cell volume expansion as compared to H-free alloy of 5.2% and 18.3%, respectively. A common feature for both phases is the anisotropic Debye–Waller factors for Ni atoms, which exhibits very high values along the *a*-axis (β_{11}). Such unusual displacement factor may be interpreted as the hint for lower space symmetry in the structure of the martensitic hydrides. Subgroups of lower symmetry have been checked but do not lead to more reliable solutions. For instance, refinements in the non-isomorphic monoclinic subgroup $P2_1/m$, the original symmetry of the martensitic alloy, were undertaken. This symmetry reduction breaks the mirror plane perpendicular to the *a*-axis, allowing the Ni atom (located at (0, y, 1/4) in *Cmcm* space group) to move out of the mirror plane ((x, 1/4, z) in $P2_1/m$ space group) in order to diminish the thermal displacement. However no improvement is obtained unless a highly anisotropic displacement factor for the Ni-atom along the *a*-axis of the monoclinic symmetry is allowed.

The β-phase is a monodeuteride. The deuterium atoms (D1) are located at 4*c* sites ($y = 0.7867$) with full occupancy. This site is tetrahedrally coordinated by four (Ti,Zr) pseudo-atoms as shown in Fig. 9a. The site radius available for deuterium is of 0.58 Å and the distance to the nearest D-atom is of 2.66 Å. The displacement factor of deuterium is rather large (3.8 Å^2), which may indicate a significant deuterium delocalization within the large hole radius.

The γ-phase is non-stoichiometric with composition $Ti_{0.64}Zr_{0.36}NiD_{2.62(2)}$. Deuterium is located in two sites D2 and D3, which are different from D1 location (Fig. 9b). D2 fully occupies 8*f* site. This site is tetrahedrally coordinated by three (Ti,Zr) and one Ni atoms. The site radius for D2 is 0.45 Å and closest distances to D2 and D3 atoms are 2.05 and 2.31 Å, respectively. D3 atoms partially occupy (62%) a 4*c* site with $y = 0.932$. This is a distorted pyramidal site for which the D3 atom is surrounded by two close Ni atoms and three distant (Zr,Ti) atoms. The site

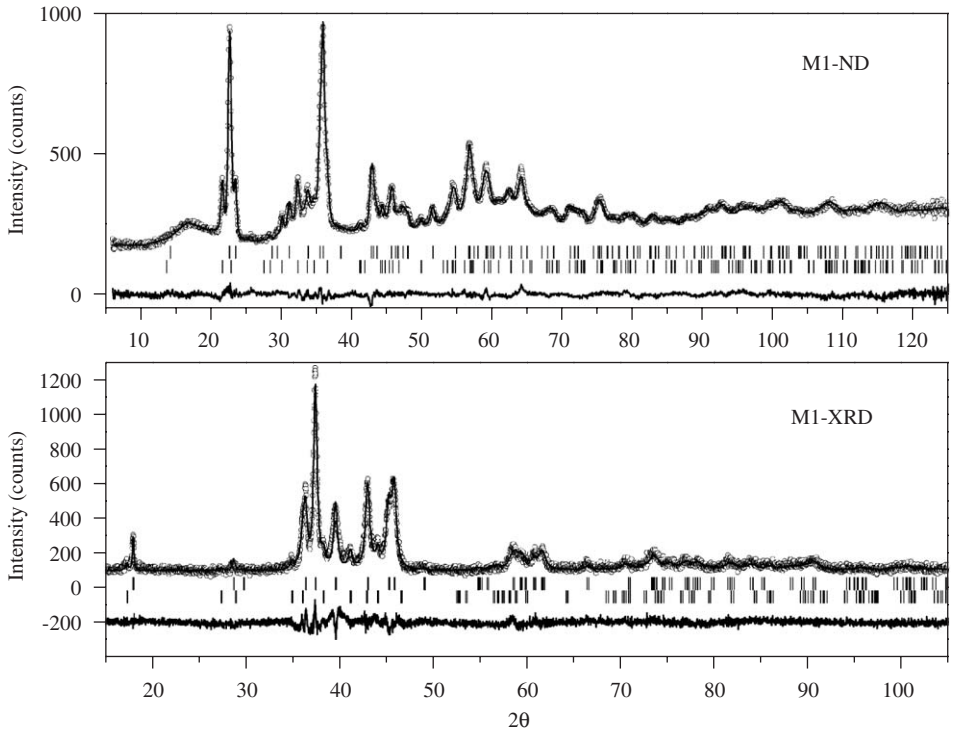

Fig. 7. Conjoint ND and XRD Rietveld analysis of martensitic $Ti_{0.64}Zr_{0.36}NiD_{1.3}$ sample (M1). Calculated diffraction pattern (continuous line), diffraction line positions (vertical bars) and difference curve at the same scale (below) are given.

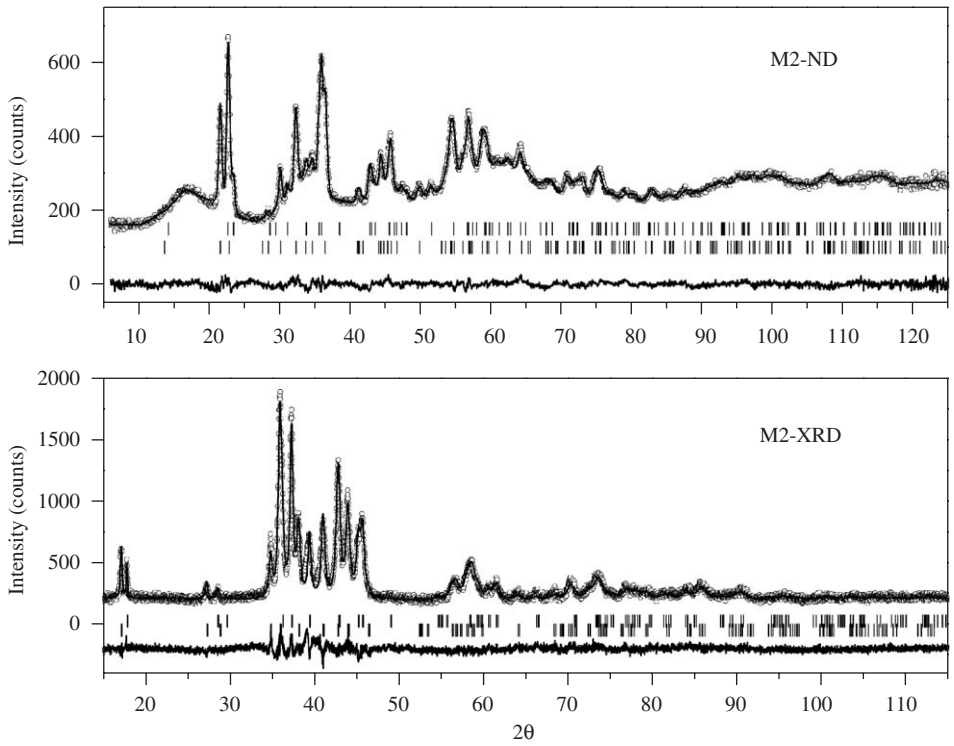

Fig. 8. Conjoint ND and XRD Rietveld analysis of martensitic $Ti_{0.64}Zr_{0.36}NiD_{1.8}$ sample (M2). Calculated diffraction pattern (continuous line), diffraction line positions (vertical bars) and difference curve at the same scale (below) are given.

radius towards Ni atoms is of 0.38 Å, whereas that towards (Zr,Ti) atoms is as much as 0.70 Å. The distance between two adjacent D3 atoms is 2.52 Å.

As concerns the structural determination for the M3 sample, the conjoint XRD–ND Rietveld analysis is shown in Fig. 10 and the results are summarized in Table 4. The

Table 3
Results of Rietveld analyses for M2 sample

Atom	Site	x	y	z	B (Å^2)	occ
β-phase, weight fraction: 46(2)%						
Ni	4*c*	0	0.4266(3)	1/4	2.9*	4 (fixed)
Ti	4*c*	0	0.1481(4)	1/4	1.6(2)	2.56 (fixed)
Zr	4*c*	0	0.1481(4)	1/4	1.6(2)	1.44 (fixed)
D1	4*c*	0	0.7867(9)	1/4	3.8(2)	4 (fixed)
	*Anisotropic $B_{Ni}(\times 10^4)$: $\beta_{11} = 2000(100)$, $\beta_{22} = 11(4)$, $\beta_{33} = 22(20)$					
Cmcm, $Z = 4$			$a = 3.1595(5)$ Å, $b = 9.901(2)$ Å, $c = 4.0075(6)$ Å, $V = 125.36(4)$ Å^3			
γ-phase, weight fraction: 54(2)%						
Ni	4*c*	0	0.4325(2)	1/4	2.2*	4 (fixed)
Ti	4*c*	0	0.1439(3)	1/4	0.9(2)	2.56 (fixed)
Zr	4*c*	0	0.1439(3)	1/4	0.9(2)	1.44 (fixed)
D2	8*f*	0	0.3109(5)	0.503(1)	2.24(8)	8 (fixed)
D3	4*c*	0	0.932(1)	1/4	2.24(8)	2.48 (5)
	*Anisotropic $B_{Ni}(\times 10^4)$: $\beta_{11} = 1440(50)$, $\beta_{22} = 8(3)$, $\beta_{33} = 43(16)$					
Cmcm, $Z = 4$			$a = 3.2414(5)$ Å, $b = 10.286(1)$ Å, $c = 4.2244(6)$ Å, $V = 140.85(4)$ Å^3			

	R_{wp}	R_p	$R_{B\beta}$	$R_{B\gamma}$	χ^2	$N_{ref\beta}$	$N_{ref\gamma}$
ND	2.35	1.97	6.49	6.02	2.05	144	165
XRD	7.75	6.04	7.79	7.49	1.75	67	74
50 variables							

Structural data on β-$Ti_{0.64}Zr_{0.36}NiD$ and γ-$Ti_{0.64}Zr_{0.36}NiD_{2.6}$ deuteride phases.
Atomic coordinates (x, y, z), isotropic (B) and anisotropic (β_{ii}) displacement factors, occupancy factors (occ) and reliability factors (R_{wp}, R_p, R_B and χ^2). Standard deviations referred to the last significant digits are given in parentheses.

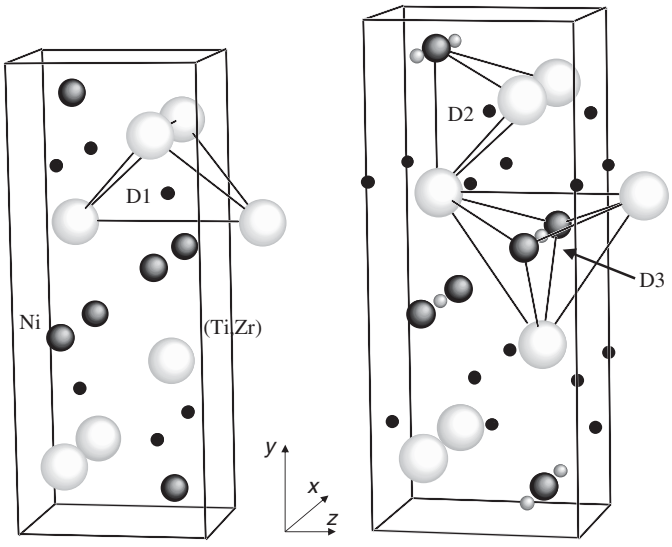

Fig. 9. Crystal structures of martensitic (a) $Ti_{0.64}Zr_{0.36}NiD_1$ deuteride and (b) $Ti_{0.64}Zr_{0.36}NiD_{2.6}$ deuteride. One (Ti, Zr) atom from an adjacent unit cell has been included to show the coordination of D atoms. The site D3 is partially occupied.

sample is single phase with orthorhombic symmetry (SG *Cmcm*). The structure resembles to that of the γ-deuteride phase with an additional site for deuterium, D4 (Fig. 11), and a larger unit-cell volume. In fact, this result points towards deuterium solution within the γ-deuteride phase as it is expected from the sloping branch in the PCI curve (Fig. 3). D4 atoms are located at 4*a* sites, which are octahedrally coordinated by four Ni atoms and two (Ti,Zr) atoms. Their closer distances to D2–D4 atoms are 2.53, 1.27 and 2.14 Å, respectively. On the basis of the Switendick criterion, this excludes the simultaneous occupation of D3 and D4 sites. However, deuterium location in these sites is allowed since D3 and D4 sites are partially occupied at 64% and 18%, respectively. The distance to (Ti,Zr) atoms is much shorter (1.85 Å) than that to Ni atoms (2.07 Å) which results in a smaller site radius for D4 towards the (Ti,Zr) atoms, 0.33 Å, than towards Ni atoms, 0.83 Å. The refined deuterium content ($D/AB = 2.81(1)$) is in agreement with the volumetric measurements ($D/AB = 2.75(5)$).

4. Discussion

4.1. Crystal structure of the deuterides

The crystal structures of $Ti_{0.64}Zr_{0.36}Ni$ deuterides are related to the parent structures of the alloy. The crystal symmetry of austenite is not modified during deuteration. This result differs from the behavior of binary TiNi alloy in the austenitic state, which undergoes a tetragonal distortion upon hydrogen absorption [19]. The absence of this distortion is probably due to the chemical disorder caused by the Zr-substitution. In fact, such disorder is reflected by the high displacement B factor of Ni ($B_{Ni} = 6.1$ Å^2) that can be attributed to a random variation of the local

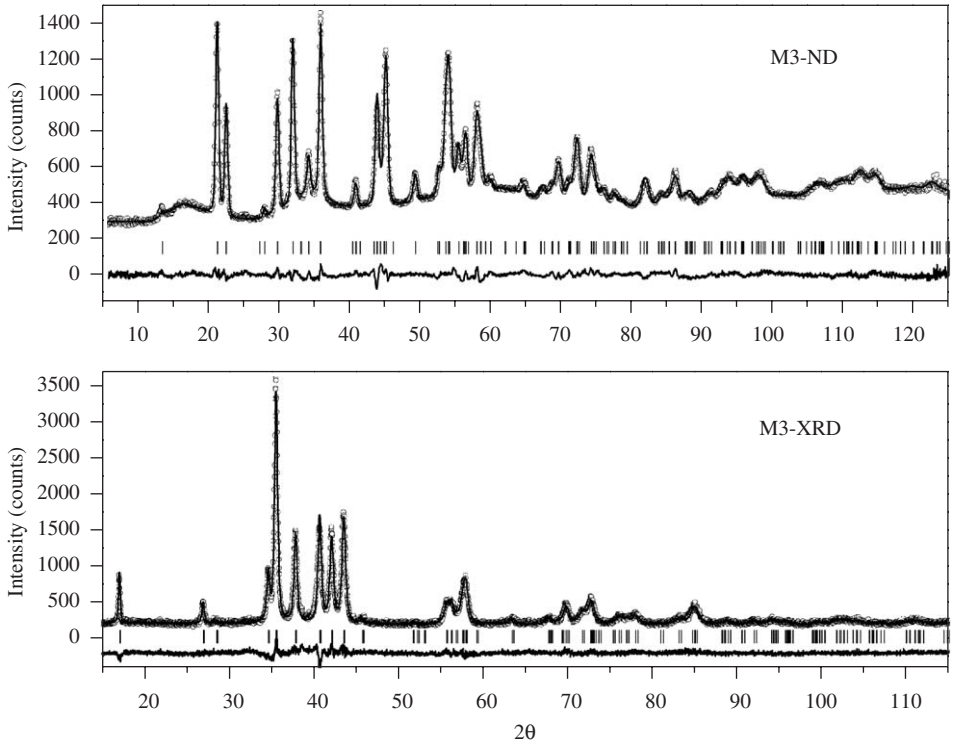

Fig. 10. Conjoint ND and XRD Rietveld analysis of martensitic $Ti_{0.64}Zr_{0.36}NiD_{2.75}$ sample (M3). Calculated diffraction pattern (continuous line), diffraction line positions (vertical bars) and difference curve at the same scale (below) are given.

Table 4
Structural data for martensitic $Ti_{0.64}Zr_{0.36}NiD_{2.8}$ γ-deuteride (M3 sample)

Atom	Site	x	y	z	B (Å^2)	Occ
Solution of D in γ-phase						
Ni	4*c*	0	0.4327(1)	1/4	2.1*	4 (fixed)
Ti	4*c*	0	0.1460(2)	1/4	0.36(9)	2.56 (fixed)
Zr	4*c*	0	0.1460(2)	1/4	0.36(9)	1.44 (fixed)
D2	8*f*	0	0.3126(5)	0.5035(3)	1.44(2)	8 (fixed)
D3	4*c*	0	0.9347(4)	1/4	1.44(2)	2.55 (2)
D4	4*a*	0	0	0	1.44(2)	0.71 (2)
	*Anisotropic $B_{Ni}(\times 10^4)$: $\beta_{11} = 1226(20)$, $\beta_{22} = 17(1)$, $\beta_{33} = 52(6)$					
Cmcm, $Z = 4$			$a = 3.2697(2)$ Å, $b = 10.3447(7)$ Å, $c = 4.2854(3)$ Å, $V = 144.95(2)$ Å^3			
	R_{wp}	R_p	R_B	χ^2	N_{ref}	
ND	2.51	2.01	4.57	4.17	165	
XRD	7.75	5.77	5.75	1.67	75	
31 variables						

Atomic coordinates (x, y, z), isotropic (B) and anisotropic (β_{ii}) displacement factors, occupancy factors and reliability factors (R_{wp}, R_p, R_B and χ^2). Standard deviations referred to the last significant digits are given in parentheses.

configuration of the neighboring Ti and Zr atoms around the Ni position. As for the martensitic alloy, it changes from monoclinic ($P2_1/m$) to base centered orthorhombic (*Cmcm*). However, this transformation can be easily achieved through a slight distortion of the beta angle in the parent alloy from 103.75° to 108.17°. To this respect, a recent study, based on density functional calculations, states that the stable structure of TiNi alloy at room temperature is *Cmcm*, being the monoclinic structure stabilized by residual internal stress [30].

The deuterium content of the β-austenitic deuteride is found to be $1.5\,D/AB$ as a result of statistical half-occupancy in 3*d* sites. Such a partial occupancy can be explained by a conjugated effect of both geometrical and electronic restrictions. Since the hole radius between Ni atoms is small (0.35 Å), the D atoms are forced to

delocalize within the plane defined by the Zr atoms. This shortens the distance between neighboring D atoms (2.25 Å) below the Switendick criterion (2.1 Å) and, therefore, impedes simultaneous occupation of two adjacent deuterium atoms located in 3*d* sites.

The crystal structures of the martensitic deuterides have many common features to those reported for the ZrNi compound. After Westlake [31], the ZrNi alloy with a CrB-type structure forms two stoichiometric hydrides (β and γ) with compositions ZrNiH and $ZrNiH_3$. For the monohydride, the D1 site is fully occupied and the metal sublattice is observed to distort from the orthorhombic to a triclinic structure. For the trihydride, both D2 and D3 sites are fully occupied and the lattice reverts to the orthorhombic structure. No H-solubility in γ-trihydride occurs for ZrNi and, therefore, the D4 site is not occupied.

For the $Ti_{0.64}Zr_{0.36}NiD$ β-phase here reported, no peak splitting of the orthorhombic reflections is observed so that a significant triclinic distortion does not occur. Nevertheless, the displacement factor for D1 is rather large (3.8 $Å^2$) and some anisotropic peak broadening is observed. A clear peak broadening at $2\theta \sim 39.5^\circ$ is observed for the (130) XRD reflection of the β-phase in both M1 and M2 samples (see for instance, Fig. 7). This may concur with recent NMR results of Adolphi et al. [32] in ZrNiD alloy suggesting two distinct D-sites due to the triclinic distortion.

As for the $Ti_{0.64}Zr_{0.36}NiD_{2.6}$ γ-phase, it differs from the ZrNi trihydride in the partial occupation of the 4*c* pyramidal site. This can be related to the small hole radius between Ni atoms (0.38 Å) and the strong anisotropic displacement for Ni atoms. The origin of such anisotropy can be explained by the chemical disorder induced by the Zr substitution. The distance between Ni atoms lying on the *x*-direction is stretched when Zr substitutes to titanium in the pyramidal site. The hole radius is consequently enlarged for the 4*c* sites having Zr coordination, allowing deuterium occupancy, whereas it remains unchanged for pure Ti_3Ni_2 pyramidal sites. Deuterium occupancy should be then related to the degree of Zr substitution. For a random $Ti_{1-x}Zr_x$ substitution, four types of pyramidal coordination $Ti_{(3-P)}Zr_PNi_2$ with $P = 0$, 1, 2, and 3 can be envisaged, being the fractional number of type-*P* sites, $f_P(x)$, given by the binomial distribution:

$$f_P(x) = \binom{3}{P} x^P (1-x)^{3-P}. \quad (1)$$

For $x = 0.36$, the fractional numbers are equal to 0.262, 0.442, 0.249 and 0.047 for Ti_3Ni_2, Ti_2ZrNi_2, $TiZr_2Ni_2$ and Zr_3Ni_2 pyramidal sites, respectively. Since the partial occupancy for D3 atoms in the γ-deuteride is 62%, this requires that the occupancy is allowed in sites coordinated by zirconium atoms ($P = 1$, 2 and 3). Moreover, deuterium solubility in γ-deuteride through partial occupation of 4*a* sites (D4), which is not observed in ZrNi alloy, will be possible when deuterium does not occupy 4*c* sites (D3).

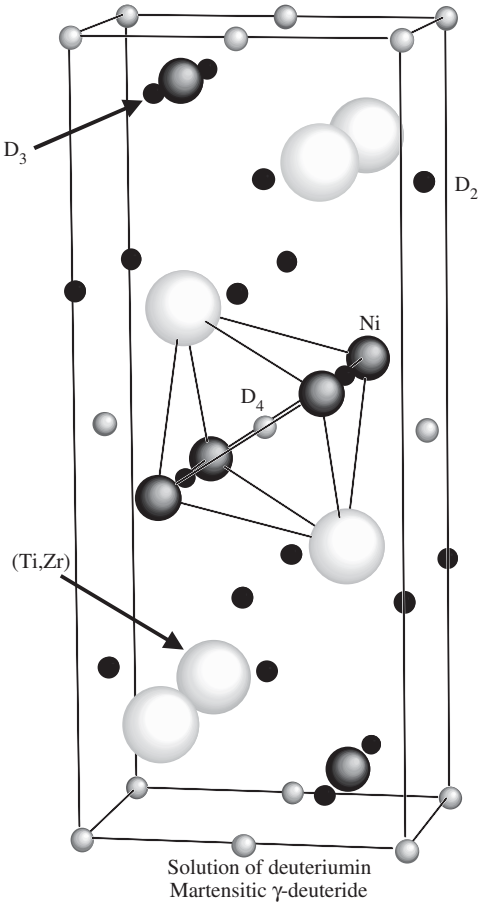

Fig. 11. Crystal structure of martensitic $Ti_{0.64}Zr_{0.36}NiD_{2.8}$ deuteride. The sites D3 and D4 are partially occupied.

This will occur when 4*c* sites are only coordinated by Ti and Ni atoms ($P = 0$). The observed occupancy, 18%, is compatible with the fractional number of Ti_3Ni_2 sites (26.2%). This statistical model is also consistent with the lack of over-stoichiometry in $ZrNiH_3$ hydride and allows the formation of a dihydride for martensitic TiNi alloy. The last prediction is, however, uncertain since the distance between adjacent D2 atoms in $Ti_{0.64}Zr_{0.36}NiD_{2.6}$ is quite short (2.05 Å). Lowering of the Zr-content may restrain full occupancy of the 8*f* site.

4.2. Deuterium-induced cell-volume changes

The unit-cell volume of both austenitic and martensitic alloys increases, as expected though distinctly, upon deuterium absorption (Fig. 12). For the austenite, the formation of $Ti_{0.64}Zr_{0.36}NiD_{1.5}$ deuteride (α'-phase) produces a volume expansion of 10.4% as compared to D-free alloy (α-phase). This expansion is thought to occur gradually since no phase transformation takes place after deuterium absorption and no plateau pressure is observed in the PCI curve (Fig. 3). On the contrary, deuterium absorption in martensitic alloy (α-phase) follows a stepwise behavior. The formation of the monodeuteride (β-phase)

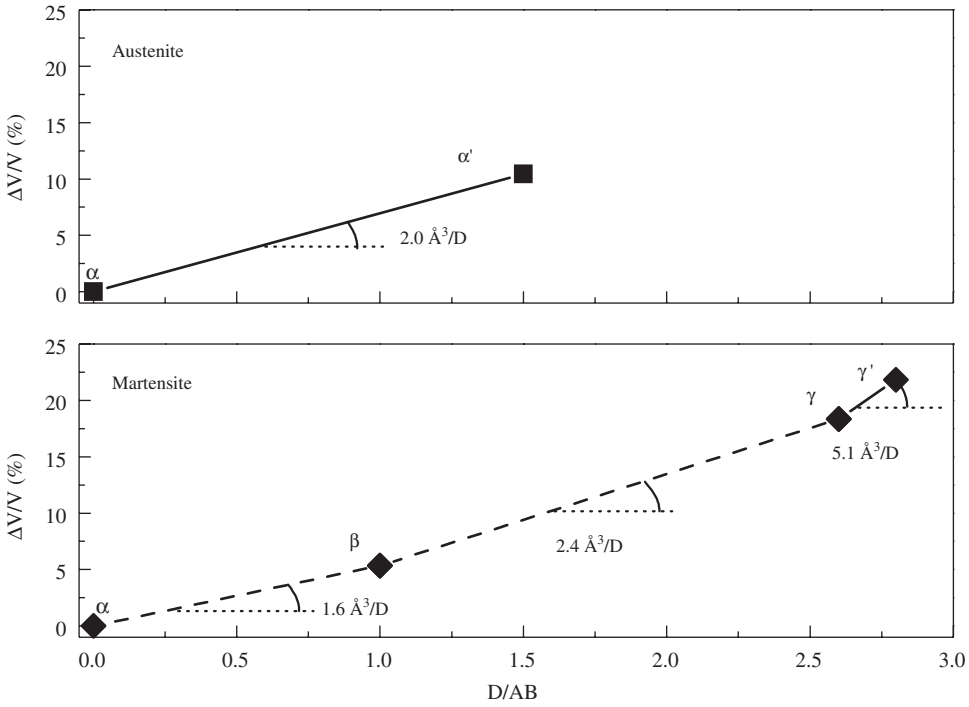

Fig. 12. Cell-volume expansion of austenitic (top) and martensitic (bottom) $Ti_{0.64}Zr_{0.36}Ni$ alloys as a function of deuterium content. Single- and two-phase regions are indicated by continuous and dashed lines, respectively. Cell-volume expansions per deuterium atom for the different phases are expressly shown.

leads to a discrete volume expansion of 5.3% and that of the over-stoichiometric dideuteride (γ-phase) to a discrete change of 12.3% between β and γ phases. Finally, deuterium solution (γ'-phase) in the γ-phase occurs gradually to complete, at $D/AB = 2.8$, an overall cell volume expansion of 21.8% with respect to the D-free alloy (α-phase). The occurrence of discrete volume changes during the phase transformation, especially between the β and γ phases, results in severe mechanical stresses at the biphasic interfaces and produces the decrepitation of the martensitic alloy. Decrepitation is not observed for the austenite in agreement with its solid solution behavior towards hydrogen absorption.

Fig. 12 shows the deuterium-induced volume change, normalized to deuterium atom, for the different phases. The values deviate significantly from the empirical rule of $v_H = 2.8 \pm 0.2\,Å^3$ per H atom observed for many metals and intermetallic compounds. For the austenite, the deuterium-induced volume is smaller ($2.0\,Å^3$/D) in agreement with other systems in which hydrogen occupies octahedral sites [33]. As for the martensite, the hydrogen-induced volume is rather small for the β-phase ($1.6\,Å^3$/D) whereas is very high for the deuterium solution in the γ-phase. This can be understood by geometrical reasons. Deuterium occupies very large holes in the first case (site hole radius 0.58 Å for D1) while it lies in small interstitial sites for the second one (site hole radius of 0.38 Å towards Ti atoms for D4). The second configuration requires a much higher displacement of the metal atoms to accommodate the deuterium occupancy.

5. Conclusions

The crystal structures of the deuterides derived from austenitic and martensitic $Ti_{0.64}Zr_{0.36}Ni$ alloy have been determined. Austenitic alloy forms a $Ti_{0.64}Zr_{0.36}NiD_{1.5}$ deuteride preserving the original cubic symmetry. On the contrary, deuterium absorption in martensite results in the transformation of the parent monoclinic structure into an orthorhombic one. Depending on the deuterium pressure, two deuteride phases can be obtained in the martensitic alloy at room temperature. At low pressures ($P < 10^3$ Pa) a stoichiometric monodeuteride, isostructural with ZrNiD deuteride, is formed. At higher pressures, an over-stoichiometric dideuteride occurs due to the incomplete occupancy of pyramidally coordinated 4*c* sites. The non-stoichiometry of this phase is related to the degree of Zr-substitution. A statistical model is proposed to account for this relationship and for the deuterium solution within the over-stoichiometric dideuteride. Further research on the structure of martensitic (Ti,Zr)Ni hydrides with distinct Zr contents is desirable to validate this model. This study shows that Zr substitution in TiNi alloy has prominent effects not only on their shape memory properties but also on their structural and hydrogenation properties.

Acknowledgments

The authors wish to thank P. Ochin (CECM-CNRS, France) for the preparation of melt-spun samples, E. Leroy

for EPMA analysis and F. Briaucourt and B. Rieu for technical assistance.

References

[1] K. Otsuka, X. Ren, Intermetallics 7 (1999) 511–528.
[2] J. Van Humbeeck, Adv. Eng. Mater. 3 (2001) 837–850.
[3] E.W. Justi, H.H. Ewe, A.W. Kalberlah, N.M. Saridakis, M.H. Schaefer, Energy Conversion 10 (1970) 183–187.
[4] D. Fruchart, J.-L. Soubeyroux, S. Miraglia, S. Obbade, G. Lorthioir, F. Basile, D. Colin, F. Faudot, P. Ochin, A. Dezellus, Z. Phys. Chem. 179 (1993) 225.
[5] K. Otsuka, T. Sawamura, K. Shimizu, Phys. Status Solidi A 5 (1971) 457–470.
[6] G.D. Sandrock, A.J. Perkins, R.F. Heheman, Metall. Trans. 2 (1971) 2769–2781.
[7] J.-L. Murray, in: J.-L. Murray (Ed.), Phase Diagrams of Binary Titanium Alloys, ASM International, Metals Park, OH, 1987, p. 197.
[8] K.H. Eckelmeyer, Scripta Metall. 10 (1976) 667.
[9] P. Olier, F. Barcelo, J.L. Bechade, J.C. Brachet, E. Lefevre, G. Guenin, J. Phys. IV France 7 (1997) C5-143–148.
[10] Y. Liu, G.S. Tan, Intermetallics 8 (2000) 67–75.
[11] S. Miyazaki, Y. Igo, K. Otsuka, Acta Metall. 34 (1986) 2045–2051.
[12] E. Dwight, Trans. AIME 215 (1959) 283.
[13] W. Bührer, R. Gotthardt, A. Kulik, O. Mercier, F. Staub, J. Phys. F, J. Phys. F Met. Phys. 13 (1983) L77–L81.
[14] G.M. Michal, R. Sinclair, Acta Crystallogr. B 37 (1981) 1803–1807.
[15] R. Schmidt, M. Schlereth, H. Wipf, W. Assmus, M. Müllner, J. Phys.: Condens. Matter 1 (1989) 2473.
[16] Y. Kudoh, M. Tokonami, S. Miyazaki, K. Otsuka, Acta Metall. 33 (1985) 2049.
[17] R. Burch, N.B. Mason, J. Chem. Soc. Faraday Trans. I 75 (1979) 561–577.
[18] D. Noréus, P.-E. Werner, K. Alasafi, E. Schmidt-Ihn, Int. J. Hydrogen Energy 10 (1985) 547.
[19] J.-L. Soubeyroux, D. Fruchart, G. Lorthioir, P. Ochin, D. Colin, J. Alloys Compd. 196 (1993) 127.
[20] I.A. Stepanov, Y.M. Flomenblit, V.A. Zaymovskiy, Phys. Met. Metallogr. 55 (1983) 180–182.
[21] F. Cuevas, M. Latroche, P. Ochin, A. Dezellus, J.-F. Fernandez, C. Sanchez, A. Percheron-Guégan, J. Alloys Compd. 330–332 (2002) 250–255.
[22] S.S. Sidhu, L. Heaton, M.H. Mueller, J. Appl. Phys. 30 (1959) 1323–1340.
[23] F. Cuevas, M. Latroche, A. Percheron-Guegan, International Symposium on Metal–Hydrogen Systems, Cracow, 5–10 September, 2004, J. Alloys Compd. 404–406 (2005) 545–549.
[24] F. Cuevas, M. Latroche, P. Ochin, A. Dezellus, A. Percheron-Guégan, J. Alloys Compd. 356–357 (2003) 730–733.
[25] J. Rodríguez-Carvajal, Physica B 192 (1993) 55–69.
[26] A.C. Switendick, Z. Phys. Chem. Neue Folge 117 (1979) 89–112.
[27] D.G. Westlake, J. Less-Common Met. 90 (1983) 251–273.
[28] S.F. Hsieh, S.K. Wu, J. Alloys Compd. 270 (1998) 237–241.
[29] J. Rodríguez-Carvajal, M.T. Fernández-Díaz, J.L. Martínez, J. Phys.: Condens. Matter 3 (1991) 3215–3234.
[30] X. Huang, G.J. Ackland, K.M. Rabe, Nat. Mater. 2 (2003) 307–311.
[31] D.G. Westlake, J. Less-Common Met. 75 (1980) 177–185.
[32] N.L. Adolphi, S. Badola, L.A. Browder, R.C. Bowman Jr., Phys. Rev. B 65 (2002) 24301–24309.
[33] Y. Fukai, The Metal–hydrogen System, vol. 21, Springer, Berlin, 1992, pp. 95–100.